RESEARCH

Covalent Bonding Enhanced Polypropylene Based T-ZIF-8 Masterbatch with Superior Photocatalytic and Antibacterial Performances

Qian Zhang[1] · Qikai Qiao[1] · Zihao Wang[3] · Yuanyuan Liu[1] · Zhen Pei[1] · Jiandong Guo[4] · Pengfei Fei[1,2] · Aiqin Zhang[1,2,3] · Husheng Jia[2,3,4] · Bingshe Xu[2,3]

Abstract

In order to solve the problem of poor compatibility between modified-ZIF-8 nanoparticles and mask matrix polypropylene (PP) and melt-blown materials, in this work, PP based modified-ZIF-8 antibacterial masterbatch was prepared employing surface modification and torque blending method. IR, SEM, XRD, XPS, DSC results confirm that the antibacterial masterbatch maintains the chemical and crystal structure of modified-ZIF-8 and the thermal stability of PP. Photocatalytic performance indicates that the antibacterial masterbatch basically maintains the photoresponse range of modified-ZIF-8, has narrower band gap and the superior photocatalytic performance than that of modified-ZIF-8. The photocatalytic antibacterial mechanism of $\cdot O_2^-$ and h^+ as antibacterial active species is revealed according to the energy band structure and free radical capture experiment. The photocatalytic antibacterial activity of the antibacterial masterbatch against *Staphylococcus aureus* and *Escherichia coli* under different dosage holds that the relationship between antibacterial rate and antibacterial agent concentration conforms to Beta distribution, demonstrating second-order kinetic behavior. The antibacterial properties reach the maximum when the loading of modified-ZIF-8 is 2% of the total weight of PP and melt-blown materials. *S. aureus* and *E. coli* could be completely killed when the simulated sunlight is irradiated for 30 min. These results indicate that PP based modified-ZIF-8 antibacterial masterbatch has potential application in photocatalytic antibacterial masks.

Keywords Modified-ZIF-8 · Polypropylene · Photocatalytic performance · Antibacterial kinetics · Antibacterial mechanism

1 Introduction

The continuous outbreak and its variation of COVID-19 seriously endanger public safety [1, 2], and the demand for masks has risen sharply. However, ordinary medical masks

Qian Zhang and Qikai Qiao have contributed equally to this research.

✉ Aiqin Zhang
ZAQ6014567@126.com

1 College of Textile Engineering, Taiyuan University of Technology, Taiyuan 030006, China

2 Shanxi-Zheda Institute of Advanced Materials and Chemical Engineering, Taiyuan 030600, China

3 Key Laboratory of Interface Science and Engineering in Advanced Materials of Ministry of Education, Taiyuan University of Technology, Taiyuan 030024, China

4 College of Materials Science and Engineering, Taiyuan University of Technology, Taiyuan 030024, China

do not have the function of antibacterial and self-cleaning, and there are problems that they cannot be recycled and produce secondary pollution after being discarded. Existing antibacterial masks use silver, graphene and traditional photocatalyst as antibacterial agents. Silver has excellent antibacterial performance, but the cost is high and easy to dissolve [3–5], graphene is easy to fall off and cause early pulmonary toxicity when inhaled into human body, and the narrow light responses range of traditional photocatalyst materials leads to low antibacterial rate under visible light.

Compared with traditional photocatalyst bacterial materials, metal organic framework materials (MOFs) have the characteristics of large specific surface area, high porosity, controllable structure and high antibacterial activity [6–10], becoming the third generation of new photocatalyst antibacterial agents. 2-Methylimidazole zinc salt (abbreviated as ZIF-8) stands out from MOFs because of its low cost, low biological toxicity, strong antibacterial activity and other characteristics [11, 12]. It can decompose the toxin produced by dead bacteria into non-toxic small molecule CO_2 and

H_2O, to achieve self-cleaning and antibacterial effect, and become the first choice of antibacterial agent for antibacterial masks [13].

Cheng et al. [14] in-situ grew ZIF-8 on the surface of cotton fabric treated with polydopamine to produce a ZIF-8/cotton fabric composite with high stability, reusability and excellent antibacterial performance. Swihart et al. [15] prepared a Cu@ZIF-8 nanowire antibacterial masks with high hydrophobicity, high bactericidal efficiency and reusable by impregnating the composite antibacterial agent on the filter layer of the masks. Gu et al. [16] employed in situ growth method to prepare ZIF-8 nanocrystals on polymer-modified cotton fibers to obtain cotton fabrics with superhydrophobic and excellent antibacterial properties. Huang et al. [17] developed antibacterial ZIF-8/GO/PAN composite fiber membrane by combination of melt blowing and hydrothermal method. The synergistic effect of GO and ZIF-8 demonstrated strong antibacterial activity against *Escherichia coli* and *Bacillus subtilis*. Lin et al. [18] constructed PP/PVA/ZIF-8 graded fiber membrane employing melt blown and electrospun composite technology, which is expected to be used as the filter layer of antibacterial masks.

The impregnation method, melt blowing method, in situ growth method and melt blowing/electrospinning technology adopted in the above study realized the composite of ZIF-8 antibacterial agent and fabric. All of them are post-finishing technology, which are physical composite or weak bond binding. The antibacterial agent is easy to fall off and dissolve during washing, leading to antibacterial inactivation [19–21]. The pretreatment technology can blend the ZIF-8 antibacterial agent with the polymer matrix to prepare the fabric, which can solve the problem of the shedding and deactivation of the antibacterial agent. Therefore, the research on the polypropylene based ZIF-8 antibacterial masterbatch for the antibacterial mask has certain practical value.

In this work, the polypropylene based modified-ZIF-8 antibacterial masterbatch was prepared by coupling the visible light responsive modified-ZIF-8 with Al–Ti composite coupling agent, and then blending it with polypropylene and its melt-blown materials, aiming to solve the compatibility problem of the blending of ZIF-8 antibacterial agents with polypropylene matrix. Its structure was characterized by SEM, FT-IR and XRD. Its energy band structure and photocatalytic performance were analyzed by XPS, Mott–Schottky curve, photocurrent and free radical capture experiment. The antibacterial kinetics of the antibacterial masterbatch was emphatically investigated, and the antibacterial mechanism was analyzed.

2 Experiments

2.1 Experimental Materials

$Zn(NO_3)_2$·$6H_2O$ (99%, Sinopharm, China), 2-methylimidazole (98%, Macklin), Al–Ti composite coupling agent (OL-AT1618, Shanxi Institute of Chemical Engineering), Polypropylene (PP) and Melt-blown materials (Shandong Tianfeng New Material Co. LTD), *Escherichia coli* and *Staphylococcus aureus* (Luwei Technology, China). Peptone (Aladdin), Beef extract (Aladdin), Agar (Aoboxing, Beijing), NaCl (98%, Macklin), Na_2HPO_4 and KH_2PO_4 (98%, Shanghai Test Agent Co. LTD), *n*-Hexane (Aladdin), Anhydrous methanol (98%, Shanxi Shengfangjie Trade Co. LTD).

2.2 Preparation of ZIF-8 and T-ZIF-8

ZIF-8 was prepared with a molar ratio of $Zn(NO_3)_2$·$6H_2O$:2-methylimidazole = 1:8. The specific process is: 0.732 g of $Zn(NO_3)_2$·$6H_2O$ and 1.62 g of 2-methylimidazole were weighed and separately dissolved in 50 mL of anhydrous methanol, which of them were mixed and stirred for 1 h at room temperature. A large amount of white precipitate was generated. The system was let stand for 10 h and centrifuged at a rate of 10,000 rpm. The centrifugal solids were dried in an oven at 60 °C for 24 h to obtain the white powder (abbreviated to ZIF-8). ZIF-8 was treated in oxygen atmosphere at 200 °C for 5 h to obtain the modified-ZIF-8, which was proposed as T-ZIF-8 [13].

2.3 Preparation of T-ZIF-8-GP and ZIF-8/PP Masterbatch

A certain amount of T-ZIF-8 was weighed. Coupling agent OL-AT1618 with a mass of 1% T-ZIF-8 was weighed and dissolved in an appropriate amount of *n*-hexane solvent, which was added into T-ZIF-8 and stirred magnetically for 1 h to obtain the suspension. The suspension was centrifuged at a rate of 10,000 rpm. The solids obtained by centrifugation were dried in an oven at 70 °C for 24 h to obtain T-ZIF-8/OL-AT1618 composites, which was proposed as T-ZIF-8-G. The modification route is shown in Fig. 1. T-ZIF-8 hydrolyzes to produce abundant hydroxyl group on the surface, while the coupling agent OL-AT1618 contains active hydroxyl group [22]. The –OH on the surface of OL-AT1618 bonds covalently with the –OH on the surface of T-ZIF-8 by dehydration and condensation, and the long alkane chain in the OL-AT1618 can be entangled with the polypropylene molecular chain, which can solve the problem that the antimicrobial agent T-ZIF-8 is easy to fall off.
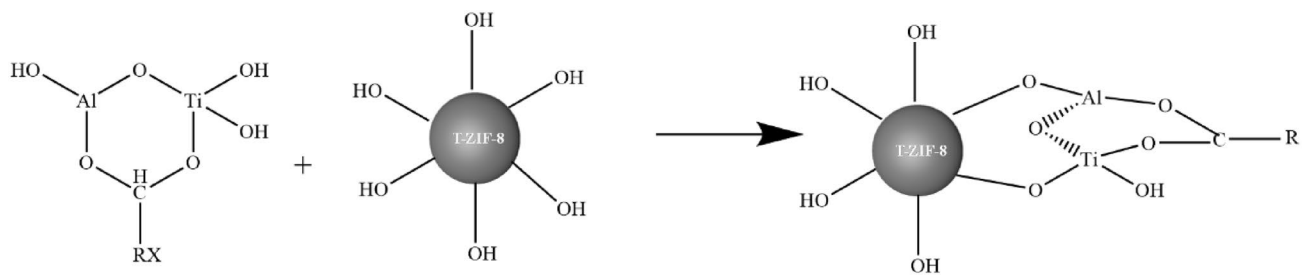
Fig. 1 The modification route of ZIF-8 by OL-AT1618

40 g polypropylene, 5 g polypropylene meltblast materials and 1.81 g T-ZIF-8-G were weighed and added into a torque rheometer, which was set at 168 °C and the rotation speed was 80 r/min. After mixing for 5 min, the polymer masterbatch is formed by granulation, which was proposed as T-ZIF-8-GP. The ZIF-8/PP masterbatch was prepared employing the method of T-ZIF-8-GP with 40 g polypropylene, 5 g polypropylene meltblast materials and 1.80 g T-ZIF-8.

2.4 Preparation of PP Based T-ZIF-8 Antibacterial Film

In order to give full play to the antibacterial effect of the antibacterial agent, maximize the specific surface area of the antibacterial agent, and achieve reuse, the experiment employed recyclable films for antibacterial experiments. The T-ZIF-8-GP antibacterial masterbatch was placed in a stainless steel mould, heated to 160 °C in the oven to the masterbatch into softening state, and pressed with the punch to the softened T-ZIF-8-GP. Finally, T-ZIF-8-GP film was obtained after cooling.

2.5 Photocatalytic Antibacterial Experiment

Staphylococcus aureus and *Escherichia coli* were selected as test strains (generation 3–9). According to the revised GB15979-2002 standard, the photocatalytic antibacterial experiment was conducted in the ultra-clean workbench.

10 g peptone, 5 g beef extract and 5 g NaCl were respectively weighed and dissolved in 1 L deionized water, and the pH value was adjusted to 7.4–7.6, which was sterilized at 121 °C for 30 min to obtain sterile culture medium. The sterile culture medium was activated in a constant temperature shaker at 37 °C and 120 rpm for 24 h to prepare bacterial stock solution.

2.84 g Na_2HPO_4 and 1.36 g KH_2PO_4 were weighed and dissolved in 1 L deionized water and sterilized to prepare sterile PBS buffer. A certain amount of bacterial stock solution was diluted 100 times with sterile culture medium, and then further diluted 100 times with PBS buffer to obtain the experimental bacterial solution. 3.5 mL of experimental bacterial solution, 50 mL of sterile PBS buffer, and an appropriate amount of T-ZIF-8-GP photocatalyst were placed and stirred for 10 min in the photocatalytic reactor. Under the irradiation of xenon lamp light source equipped with AM1.5 filter and UV total reflection plate, photocatalytic antibacterial experiment was conducted at room temperature with condense circulating water.

20 g agar powder was added to the liquid medium, sterilized, and added to the sterilized petri plate to prepare solid medium after cooling and curing. Under xenon lamp illumination, 100 μL antibacterial liquid was taken and coated evenly on sterile solid medium, which was placed in a constant temperature incubator at 37 °C for 24–48 h. Bacterial colony growth on the petri plate was photographed and counted.

$$A.R = (N_0 - N)/N_0 \times 100\%, \tag{1}$$

where A.R denotes the antimicrobial rate, N_0 the initial microbial number, N the instant microbial number.

2.6 Antibacterial Kinetics Experiment

The bactericidal sensitivity of microorganisms to antibacterial agents is used to characterize the killing ability, the microorganisms are assumed to be in a stable period regardless of microbial proliferation. When the initial microbial number N_0 in the system remains unchanged, the microbial number in the system decrease to N at time t after the addition of antibacterial agent. The relationship of them is shown as follows:

$$\ln(N/N_0) = -K_d t = -KC^n t, \tag{2}$$

where K_d denotes bactericidal rate constant. K denotes the bactericidal sensitivity coefficient of microorganisms to antimicrobials, which is related to the bactericidal capacity and performance of antimicrobials and the types of microorganisms, is the characterization of the bactericidal capacity of antimicrobials. C denotes concentration of antimicrobial agents.

Through the relationship between time t and the corresponding number of microorganisms N, the bactericidal rate constant K_d under the action of different antibacterial agent concentrations was linearly fitted. Then, different bactericidal rate K_d was used to plot different antibacterial agent concentration C, and then the antibacterial kinetic order n was fitted.

2.7 Characterization

Infrared spectra were measured in the range of 4000–400 cm^{-1} by KBr disk method using a Thermo Scientific Nicolet iS20 Fourier infrared spectrometer. The XRD pattern was measured by MiniFlex600 X-ray diffractometer. X-ray photoelectron spectroscopy was determined by Thermo Scientific K-Alpha photoelectron spectrometer. The morphology and element types of the materials were characterized by JEOL JSM-6700F field emission scanning electron microscope combined with EDS energy spectrum. UV–visible diffuse reflectance spectra were measured in the range of 200–800 nm using a PE Lambd1050 UV spectrophotometer. Photocurrent, impedance, and Mott–Schottky curve were measured using a CHI660E electrochemical workstation (CH Instruments, China). The fluorescence spectra were recorded by Hitachi F-4700 fluorescence spectrophotometer. Paramagnetic resonance spectroscopy was determined by free radical trapping assay using JES FA200 JEOL.

3 Results and Discussion

3.1 IR Spectra

In order to study the molecular structure, the infrared spectra of ZIF-8, T-ZIF-8, T-ZIF-8-G, and T-ZIF-8-GP were measured in the range of 4000–400 cm^{-1} by KBr disk, as shown in Fig. 2. It can be seen that the peak at 421 cm^{-1} is assigned to the Zn–N stretching vibration generated by the coordination of 2-methylimidazole and Zn^{2+} in ZIF-8, and the peak at 2226 cm^{-1} is attributed to the antisymmetric stretching of –N=C=O, which is consistent with the literature report [22]. Compared with T-ZIF-8, the characteristic peaks at 1581 cm^{-1} and 1668 cm^{-1} are detected in T-ZIF-8-G, corresponding to the characteristic peaks of –O–C=O connected with Ti and Al, respectively. It is due to the fact that the electron cloud density of –O–C=O decreases to result in a blueshift of the characteristic peak of –O–C=O owing to the electronic absorption of Ti, indicating the existence of coupling agent OL-AT1618. In addition, the –OH absorption peak located at 3561 cm^{-1} disappear when T-ZIF-8 is coupled to OL-AT1618, while a new broad absorption peak is probed at 549 cm^{-1}, which is attributed to
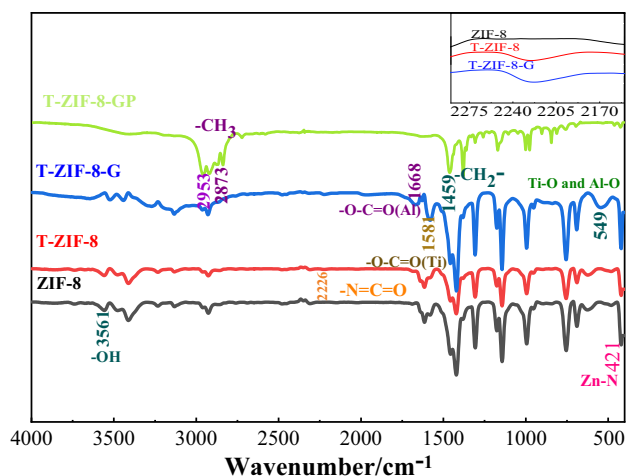

Fig. 2 IR spectra of ZIF-8, T-ZIF-8, T-ZIF-8-G and T-ZIF-8-GP

the superposition of stretching vibration of Ti–O and Al–O bond, indicating that the coupling agent bond to –OH on the surface of T-ZIF-8 through Ti and Al. In T-ZIF-8-GP, the characteristic peaks located at 2953 cm^{-1} and 2873 cm^{-1} correspond to the anti-symmetric and symmetric stretching vibration of CH$_3$ in PP respectively, and the peaks located at 2917 cm^{-1} and 2845 cm^{-1} correspond to the anti-symmetric and symmetric stretching vibration of medium CH$_2$ in PP respectively. The variable angle vibration peak of CH$_2$ in PP appears at 1459 cm^{-1}. In addition, a series of sharp absorption bands of moderate intensity are detected in the region of 1250–830 cm^{-1}, indicating that PP is arranged in a helical arrangement of isoregular molecular chains [23]. In T-ZIF-8-GP, the peak at 421 cm^{-1} is belonged to the stretching vibration of Zn–N, indicating that the molecular structure of T-ZIF-8-G keep stable after blending with PP.

3.2 Microtopography

In order to investigate the dispersion of T-ZIF-8 in PP, the morphology characteristics of PP, T-ZIF-8-GP and ZIF-8/PP film were studied by scanning electron microscope, as shown in Fig. 3a–f. Figure 3a–c display the morphology of PP at the magnification of 450, 5000 and 35,000 respectively. As can be seen from the figure, the surface of PP is relatively smooth and no doping phase is attached. When the magnification is 5000, fine crystalline orientation is observed on the surface of PP film, and the crystallization on the surface of PP is more obvious when the magnification is 35,000 times. The reason is that PP is crystallized under pressure in the melting state. Figure 3d shows the microscopic morphology of ZIF-8/PP at magnification of 35,000, it is obvious that T-ZIF-8 particles generate agglomeration in ZIF-8/PP. The microscopic morphology of T-ZIF-8-GP at magnification of 15,000 and 35,000 are presented in Fig. 3e and f. It can
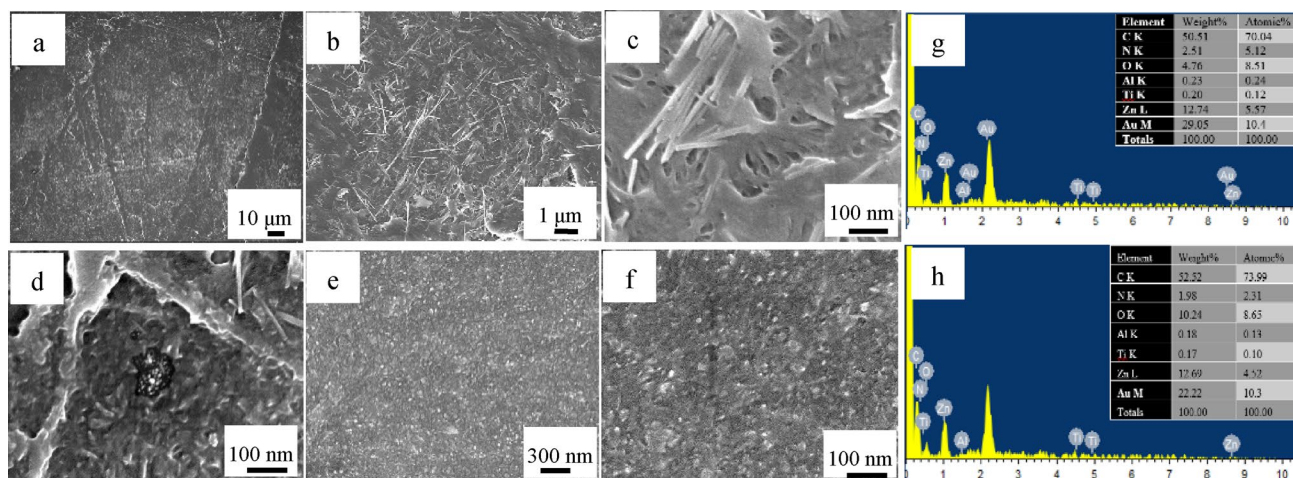
Fig. 3 SEM images of PP film (**a–c**), ZIF-8/PP (**d**), T-ZIF-8-GP (**e**, **f**) and EDS spectra of T-ZIF-8-G (**g**) and T-ZIF-8-GP (**h**)

be seen that the antibacterial agent T-ZIF-8 is more evenly dispersed in T-ZIF-8-GP, and the diameter is about 50 nm, and no agglomeration occurs, indicating that the modification of T-ZIF-8 by coupling agent solves the problem of poor dispersion of T-ZIF-8 in PP. The results suggest that T-ZIF-8 in T-ZIF-8-GP can better play a role in antibacterial application.

In order to prove the elemental composition of T-ZIF-8-G and T-ZIF-8-GP, EDS energy spectrum equipped with SEM was used for scanning, as presented in Fig. 3g, h. T-ZIF-8-G and T-ZIF-8-GP are composed of C, N, O, Zn, Al and Ti, and the element content is: $C > Zn > O > N > Al > Ti$, among which C and Zn are the main elements. Al and Ti elements confirm the existence of OL-AT1618 coupling agent, which further supports the formation of Al–O and Ti–O in T-ZIF-8-G infrared spectra.

3.3 XRD Diffraction Pattern

In order to reveal the crystal structure of T-ZIF-8 modified by OL-AT1618, the X-ray diffraction pattern of T-ZIF-8, T-ZIF-8-G and T-ZIF-8-GP were measured in the range of 5°–50° under the copper Kα radiation (λ = 1.5406) generated at 30 mA and 36 kV, as exhibited in Fig. 4. Both T-ZIF-8 and T-ZIF-8-G have diffraction peaks at 7.39°, 10.43°, 12.74°, 14.74°, 16.47° and 18.08°, corresponding to the crystal plane reflection of (011), (002), (112), (022), (013) and (222), respectively. These results maintain that the crystal structure of T-ZIF-8 is not damaged by the coupling reaction. However, the disappearance of the corresponding diffraction peak signal in T-ZIF-8-GP is due to the fact that the content of T-ZIF-8 antibacterial agent is less than 5%. The diffraction peak appears at 13.88°, 16.66°, 18.29°, 20.86° and 21.56°, corresponding to the (110), (040), (130), (111) and (131) crystal planes of PP α crystal, respectively [24].
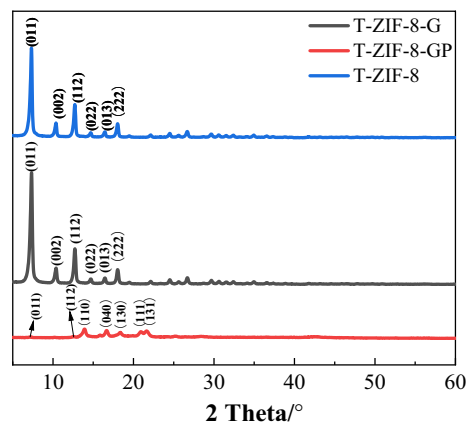

Fig. 4 XRD diffraction pattern of T-ZIF-8, T-ZIF-8-G and T-ZIF-8-GP

3.4 XPS Photoelectron Spectra

To further explore and analyze the elemental composition and valence states, the X-ray photoelectron spectra of T-ZIF-8, T-ZIF-8-G and T-ZIF-8-GP were recorded using Al-Kα rays as the excitation source, as demonstrated in Fig. 5. Wherein, the C1s high-resolution spectra of T-ZIF-8, T-ZIF-8-G and T-ZIF-8-GP are displayed in Fig. 5a, all of them have energy peaks at 284.3 eV, 284.8 eV, 285.7 eV and 287.9 eV, being belonged to the binding energies of C–C, C–N, C=O and C=C respectively. T-ZIF-8-G shows a new energy peak at 284.83e V, which corresponds to the C–O binding energy of the coupling agent OL-AT1618.The C1s high-resolution spectra of T-ZIF-8-GP is basically consistent with the T-ZIF-8-G spectra. The high-resolution spectra are shown in Fig. 5b. In T-ZIF-8-G and T-ZIF-8-GP, the energy spectrum peaks are detected at 398.4 eV and 400 eV, respectively, corresponding to the C–N and C=N binding
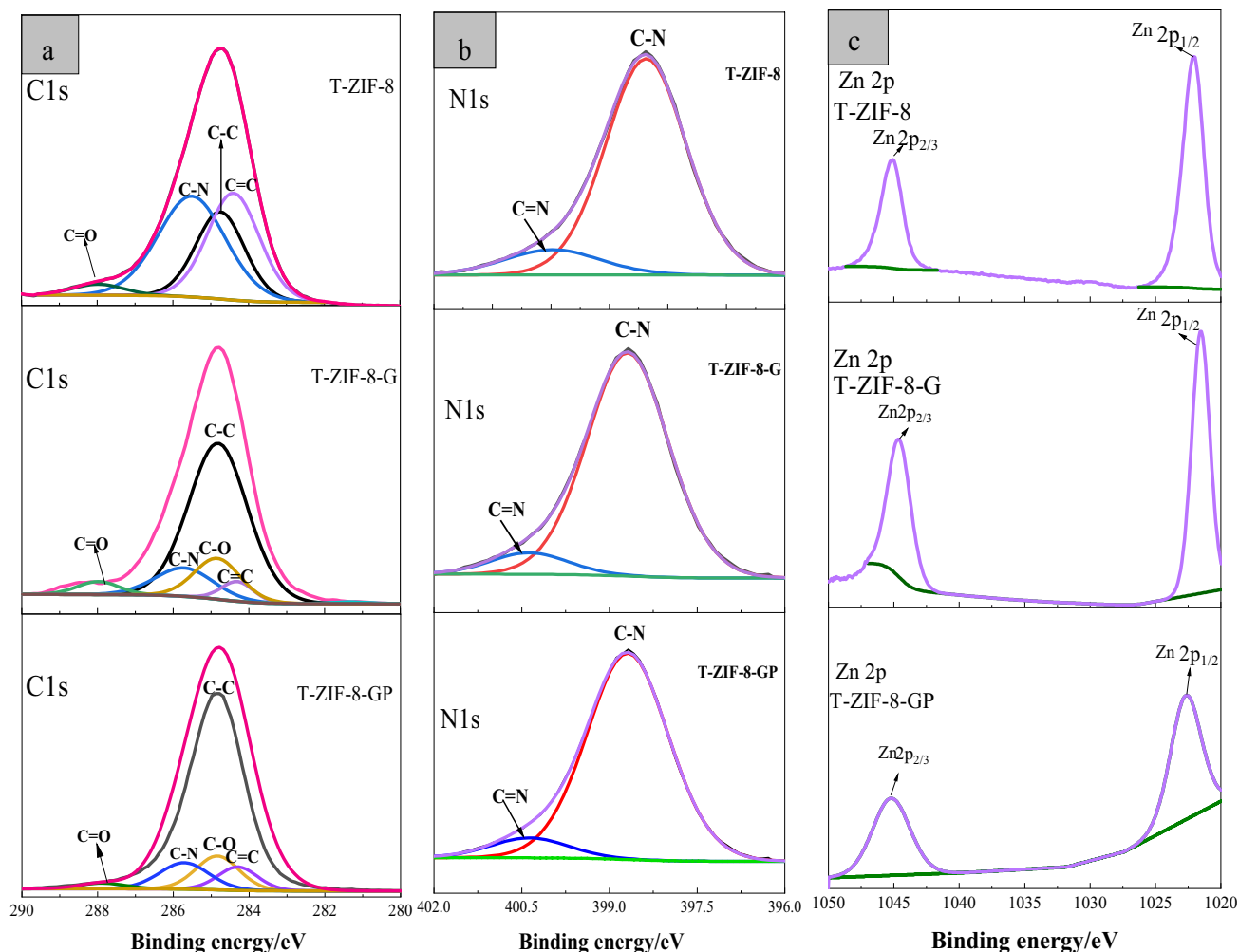
Fig. 5 XPS photoelectron spectra of T-ZIF-8, T-ZIF-8-G and T-ZIF-8-GP: C1s (**a**), N1s (**b**), Zn2p (**c**)

energy in imidazole structure. The high resolution spectra of Zn^{2+} are presented in Fig. 5c. The energy spectrum peaks of 1022 eV and 1045 eV correspond to the electron binding energy of Zn^{2+} at $2p_{3/2}$ and $2p_{1/2}$, respectively, indicating that the valence state of Zn^{2+} in T-ZIF-8-G and T-ZIF-8-GP does not change, which can ensure antimicrobial properties of T-ZIF-8.

3.5 Thermal Stability

In order to investigate the influence of T-ZIF-8-G doping on the thermal stability of PP, the DSC curves of PP, PP melt-blown materials and T-ZIF-8-GP were measured in the range of 50–200 °C at the heating rate of 10 °C/min, as presented in Fig. 6. The crystallization temperature of PP is 115 °C. After doping T-ZIF-8-G, the crystallization temperature of T-ZIF-8-GP rises to 120 °C, and the exothermic peak is sharper. The reason is that a small amount of antibacterial agent T-ZIF-8-G plays a nucleation role, which reduces
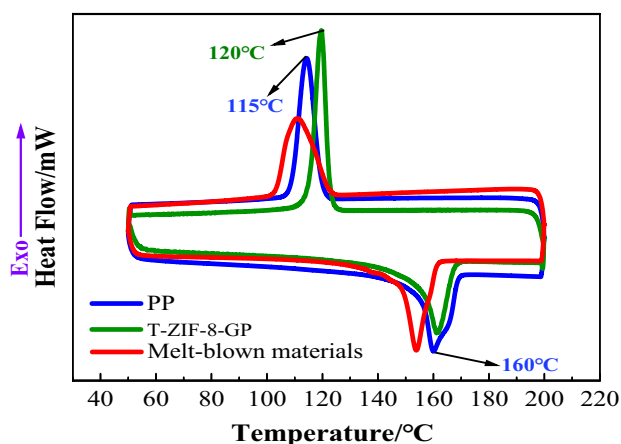

Fig. 6 DSC curves of PP, melt-blown materials and T-ZIF-8-GP

the size and density of the intramolecular crystal nucleus of PP and increases the rate of heterogeneous nucleation and crystallization, resulting in the increase of the crystallization temperature of T-ZIF-8-GP. The melting temperature of T-ZIF-8-GP is located at 160 °C in consistent with that of PP, indicating that nanoparticles T-ZIF-8 have no influence on the melting process temperature of polymer matrix PP. In addition, the melting peak height and width of T-ZIF-8-GP decrease, which is a typical characteristic of metal particle composite in polymer matrix, indicating that the nano-antibacterial agent T-ZIF-8 is successfully compounded with PP matrix [25].

3.6 Photocatalytic Properties

In order to investigate the light response range, UV–visible DRS of T-ZIF-8, T-ZIF-8-G and T-ZIF-8-GP were measured in the range of 200–800 nm, as shown in Fig. 7a. All the three substances show absorption peaks at 222 nm and 300 nm, which was mainly attributed to the fact that the ligand 2-methylimidazole contains high energy lone pair electrons. According to the principle of minimum energy, the smaller the total energy of the system, the more stable the structure is. Therefore, the lone pair electrons in the ligand are transferred to metal Zn^{2+} to realize the LMCT transition, thus reducing the total energy of the system. The absorption peaks of the three materials in the range of 340–450 nm are mainly due to the oxidation of the part $–CH_3$ in the 2-methylimidazole to –N=C=O during the heat treatment process, and the ligand structure of T-ZIF-8 is destroyed to form self-defects [26]. The optical absorption cut-off wavelength of T-ZIF-8, T-ZIF-8-G and T-ZIF-8-GP are 700 nm, 600 nm and 700 nm respectively, which indicate that the modification of T-ZIF-8 by OL-AT1618 reduces the optical response range of T-ZIF-8 to some extent. However, the light response range of T-ZIF-8-GP is widened, which is similar to that of T-ZIF-8. The results indicate that T-ZIF-8-G doped in PP still maintain the excellent light absorption performance of T-ZIF-8.

According to the UV–Vis DRS, the Tauc diagram was obtained as exhibited in Fig. 7b. As can be seen from the figure, the band gap width of T-ZIF-8, T-ZIF-8-G and T-ZIF-8-GP are 2.27 eV, 2.14 eV and 2.09 eV respectively [27], indicating that the modification of T-ZIF-8 by OL-AT1618 reduces the band gap width of T-ZIF-8. It is attributed to the fact that coupling reduces the agglomeration effect of T-ZIF-8 nanoparticles to result in the increase of the specific surface area of T-ZIF-8-G, leading to make the electrons more excited [28]. The band gap width of T-ZIF-8-GP is further reduced to 2.09 eV, which is favorable for photogenerated electrons to transition from valence band to conduction band under irradiation. Therefore, the generation

efficiency of charge carriers such as photo-generated electron–hole is improved.

In order to analyze the energy band structure of T-ZIF-8-GP, the Mott–Schottky curve was measured in the range of − 0.75 to 1 V, as presented in Fig. 7c. The result shows that T-ZIF-8-GP has flat band potential of − 0.61 eV (vs. NHE) with a positive slope, indicating that the composite T-ZIF-8-GP is belonged to N-type semiconductor. Therefore, the flat band potential can be approximately equal to the conduction band potential [29]. According to Mott–Schottky curve (MS) and Tauc diagram, the energy band structure of T-ZIF-8-GP is plotted, as shown in Fig. 7d. The valence band potential (1.48 eV) of T-ZIF-8-GP, which is lower than the oxidation potential of $H_2O/·OH$ (2.68 eV), makes it difficult to generate –OH radicals according to thermodynamic theory; the conduction band potential (− 0.61 eV) of T-ZIF-8-GP, which is greater than the reduction potential (− 0.33 eV) of $O_2/·O_2^−$, is conducive to the generation of superoxide radicals $·O_2^−$ [30]. Compared with the band gap (2.27 eV) of T-ZIF-8 [13], the band gap of T-ZIF-8-GP is reduced to 2.09 eV. The result indicates that it is easier to be driven under simulated sunlight, generate photogenerated electron $e^−$ and hole h^+, and reduce the O_2 adsorb on the surface of T-ZIF-8-GP to $·O_2^−$ [31]. In order to verify this theory, employing the DMPO as the trapping agent, electron paramagnetic resonance (EPR) spectra of T-ZIF-8-GP was measured by superoxide radicals capture experiment at 0 min, 5 min and 10 min of full light irradiation respectively, as shown in Fig. 7e. It is clear that little $·O_2^−$ signal is induced in the dark state, an obvious instantaneous $·O_2^−$ signal is captured when the full light irradiation is carried out for 5 min, and the signal intensity of $·O_2^−$ increases significantly as the illumination time is extended to 10 min. The results indicate that T-ZIF-8-GP generates superoxide radicals $·O_2^−$ with strong REDOX properties under full light irradiation, which verifies the theory that $·O_2^−$ is the main antibacterial activity species of T-ZIF-8-GP, in consistent with the analysis results of energy level structure.

The photocurrent of T-ZIF-8, T-ZIF-8-G, and T-ZIF-8-GP was measured by electrochemical workstation under 400 s all-light-no cycle, as illustrated in Fig. 7f. It can be seen from the figure that the photocurrent density of T-ZIF-8-G is approximately identical with that of T-ZIF-8, which indicates that the surface modification of T-ZIF-8 by coupling agent OL-AT1618 keep the conductivity of T-ZIF-8. The photocurrent density of T-ZIF-8-GP is significantly higher than that of T-ZIF-8, because the coupling reaction and the torque blending of T-ZIF-8-G and PP matrix overcome the agglomeration of T-ZIF-8 nanoparticles. T-ZIF-8 nanoparticles have better dispersion in T-ZIF-8-G and T-ZIF-8-GP, which increases the specific surface area of T-ZIF-8, elevates the light absorption efficiency, and finally improves the electron–hole separation efficiency [32, 33].

Fig. 7 UV–Vis DRS (**a**) and Tauc diagram (**b**) of T-ZIF-8, T-ZIF-8-G, T-ZIF-8-GP; Mott–Schottky curve of T-ZIF-8-GP (**c**); band structure of T-ZIF-8-GP (**d**); the photocurrent of T-ZIF-8, T-ZIF-8-G, and T-ZIF-8-GP (**e**); EPR spectroscopy of T-ZIF-8-GP (**f**); the fluorescence emission spectra of T-ZIF-8, T-ZIF-8-G, and T-ZIF-8-GP (**g**)
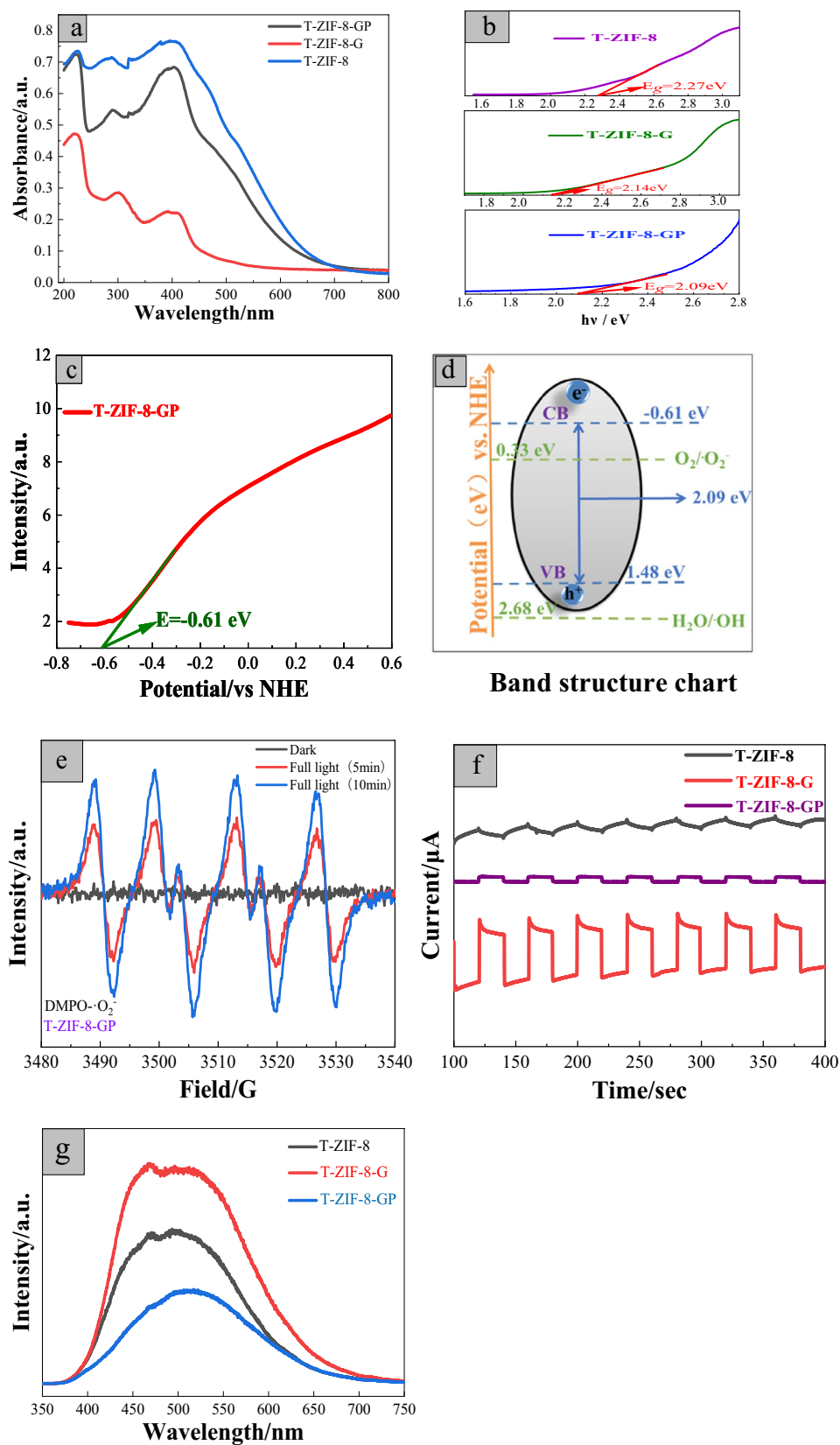
In order to regulate photocatalytic performance, it is necessary to inspect the recombination rate of electron–hole pairs. Photoluminescent spectroscopy is a good tool to evaluate the electron–hole recombination rate, electron transfer and migration under photoexcitation in semiconductors. Generally, the stronger the fluorescence emission intensity is, the higher the electron–hole recombination rate will be, resulting in the lower antibacterial efficiency of photocatalysis. In order to further investigate the electron–hole recombination rate of T-ZIF-8 modified by coupling and loaded on polypropylene matrix under light, the fluorescence emission spectra of T-ZIF-8, T-ZIF-8-G and T-ZIF-8-GP were measured with 280 nm as the excitation wavelength, as shown in Fig. 7g. It can be found that compared with T-ZIF-8, the electron–hole recombination rate of T-ZIF-8-G is enhanced in that the crystal surface of T-ZIF-8 is covered by the coupling agent OL-AT1618, which increases the electron hole recombination rate [34]. When T-ZIF-8-G is combined with PP matrix, the electron hole recombination rate of T-ZIF-8-GP is magnificently lower than that of T-ZIF-8 and T-ZIF-8-G, because isotactic polypropylene is an α crystalline substance, and the cell morphology of α crystal lead to a large number of shallow traps in isotactic polypropylene. The carrier generated in T-ZIF-8 is easier to migrate in ipp-α, which makes the electron–hole recombination rate of T-ZIF-8-GP decrease under the action of photocatalysis [35].

3.7 Antibacterial Kinetics

According to the principle of antibacterial kinetics, the concentration of T-ZIF-8 in the bacterial solution was set as 100 mg/L, 200 mg/L, 300 mg/L, 500 mg/L and 600 mg/L respectively, the antibacterial properties of T-ZIF-8-GP film were evaluated under the simulated sunlight irradiation. The antibacterial properties of T-ZIF-8-GP in dark were used as the control group under the same antibacterial concentration.

The colony photographs at the different concentration against *Staphylococcus aureus* are depicted in Fig. 8a, and the antibacterial ratio were calculated according to Eq. (1). The columnar relationship between antibacterial ratio and light irradiation time t at different antibacterial agent concentration is presented in Fig. 8b. Then ln (N/N_0) was used to make a scatter plot for the illumination time t, and the bactericidal rate K_d under different antibacterial agent concentration was obtained by linear fitting, as displayed in Fig. 8c. As can be seen from the figures, when the concentration of T-ZIF-8 in bacterial solution is 100 mg/L, 200 mg/L, 300 mg/L, 500 mg/L and 600 mg/L respectively, the corresponding bactericidal rate constant K_d is 0.1598, 0.2098, 0.1892, 0.1789 and 0.1497 respectively. That is, $K_{d2} > K_{d3} > K_{d4} > K_{d1} > K_{d5}$. The antibacterial rate achieves to maximum when the concentration of T-ZIF-8 is 200 mg/L, that is, the loading of T-ZIF-8 is 2% of the total mass of

PP and meltblown materials. The final antibacterial effect in dark under different concentration of antibacterial agent are 50.87%, 74%, 56.35%, 62.72% and 51.76%, respectively. The antibacterial rate of T-ZIF-8-GP against *Staphylococcus aureus* reaches the peak in dark when the concentration of T-ZIF-8 in bacterial solution was 200 mg/L, being consistent with that of photocatalysis antibacterial activity.

To investigate the order of antibacterial kinetics of T-ZIF-8-GP against *Staphylococcus aureus*, the concentration C of T-ZIF-8 and the antibacterial rate constant K_d were taken respectively as the independent variable and the dependent variable to fit the relationship curve, as presented in Fig. 8d. It can be seen from the figure that the fitting curve of T-ZIF-8 concentration C and K_d conforms to Beta distribution, that is, the antibacterial behavior of T-ZIF-8-GP against *Staphylococcus aureus* is second-order dynamics.

The colony photographs at the different concentration against *Escherichia coli* are shown in Fig. 9a. Then, the antibacterial rate was calculated according to Eq. (1), and the columnar relationship between antibacterial rate and light irradiation time t under different antibacterial agent concentration is presented in Fig. 9b. Then ln (N/N_0) was used to make a scatter plot for the illumination time t, and the bactericidal rate K_d under different antibacterial agent concentration was obtained by linear fitting, as shown in Fig. 9c. When the concentration of T-ZIF-8 is 100 mg/L, 200 mg/L, 300 mg/L, 500 mg/L and 600 mg/L respectively, the total inactivation time of T-ZIF-8-GP against *Escherichia coli* is 48 min, 30 min, 45 min, 55 min and 70 min, respectively. It can be concluded that when the concentration of T-ZIF-8 in bacterial solution under photocatalytic condition is 200 mg/L, that is, T-ZIF-8 is 2% of the total mass of PP and melt-blown materials, the time required by T-ZIF-8-GP to kill all the *Escherichia coli* is the shortest, in consistent with the result of *Staphylococcus aureus*.

When the concentration of T-ZIF-8 is 100 mg/L, 200 mg/L, 300 mg/L, 500 mg/L and 600 mg/L, the correlation coefficients R^2 are 0.9228, 0.8220, 0.8735, 0.9798 and 0.8865 respectively, being greater than 0.8. The results indicate that the reliability of linear fitting degree is better. The corresponding bactericidal rate constant K_d are 0.0144, 0.0526, 0.0510, 0.0498 and 0.0225 respectively. Because $K_{d2} > K_{d3} > K_{d4} > K_{d5} > K_{d1}$, when the concentration of T-ZIF-8 in bacterial solution under photocatalytic condition is 200 mg/L, that is, T-ZIF-8 is 2% of the total mass of PP and melt-blown materials, the bactericidal rate of T-ZIF-8-GP against *Escherichia coli* is the most rapid. To explore the order of antibacterial kinetics of T-ZIF-8-GP against *Escherichia coli*, the concentration C of T-ZIF-8 and the corresponding antibacterial rate constant K_d was taken respectively as the horizontal coordinate and the vertical coordinate to make a plot and fit the relationship curve, as illustrated in Fig. 9d. It is clear that the concentration C of
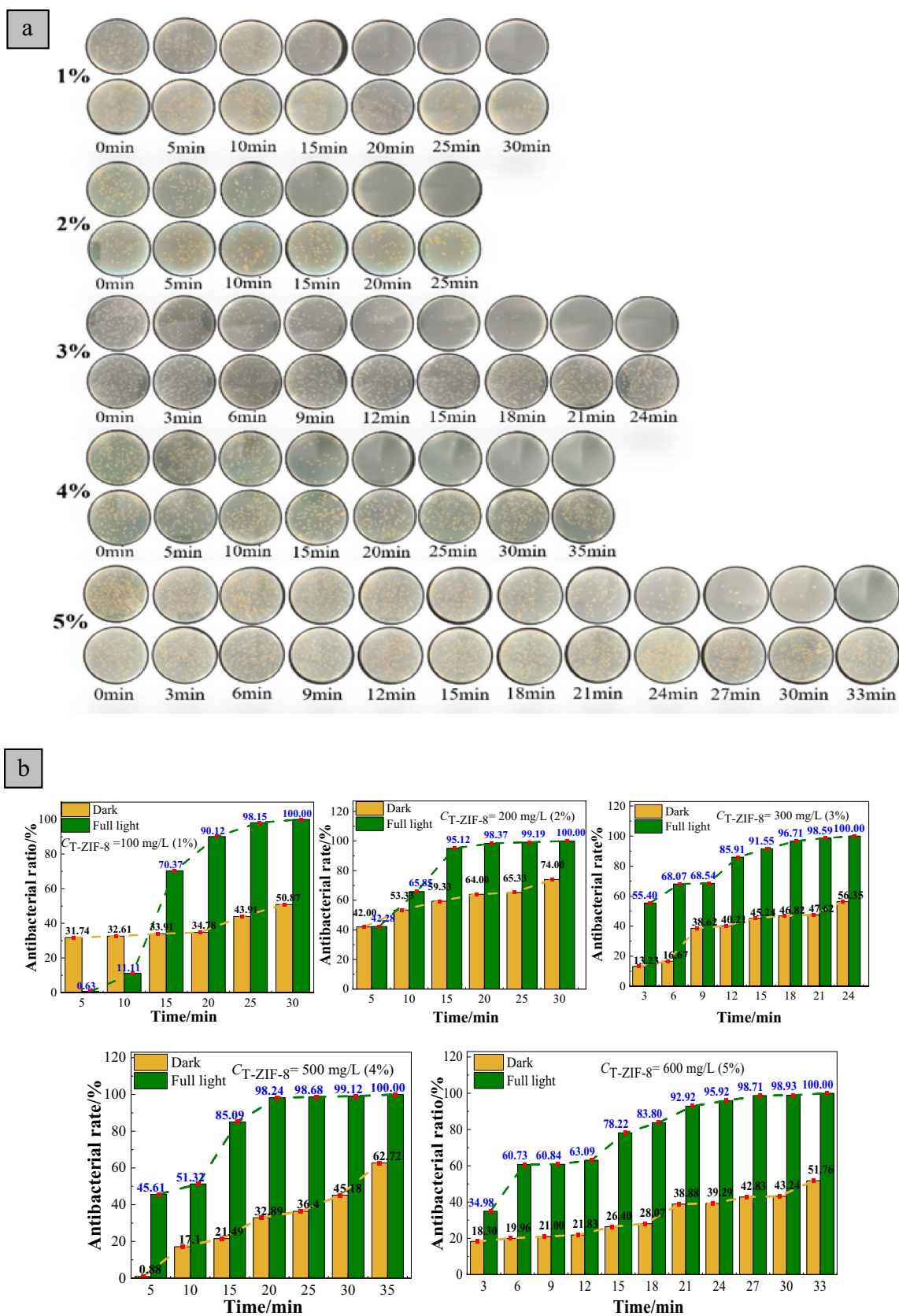
Fig. 8 Colony growth of *Staphylococcus aureus* (**a**), the antibacterial ratio against *Staphylococcus aureus* (**b**), the antimicrobial rate fitting curves (**c**) at different concentration of T-ZIF-8; the antibacterial dynamics fitting curve of T-ZIF-8-GP against *Staphylococcus aureus* (**d**)
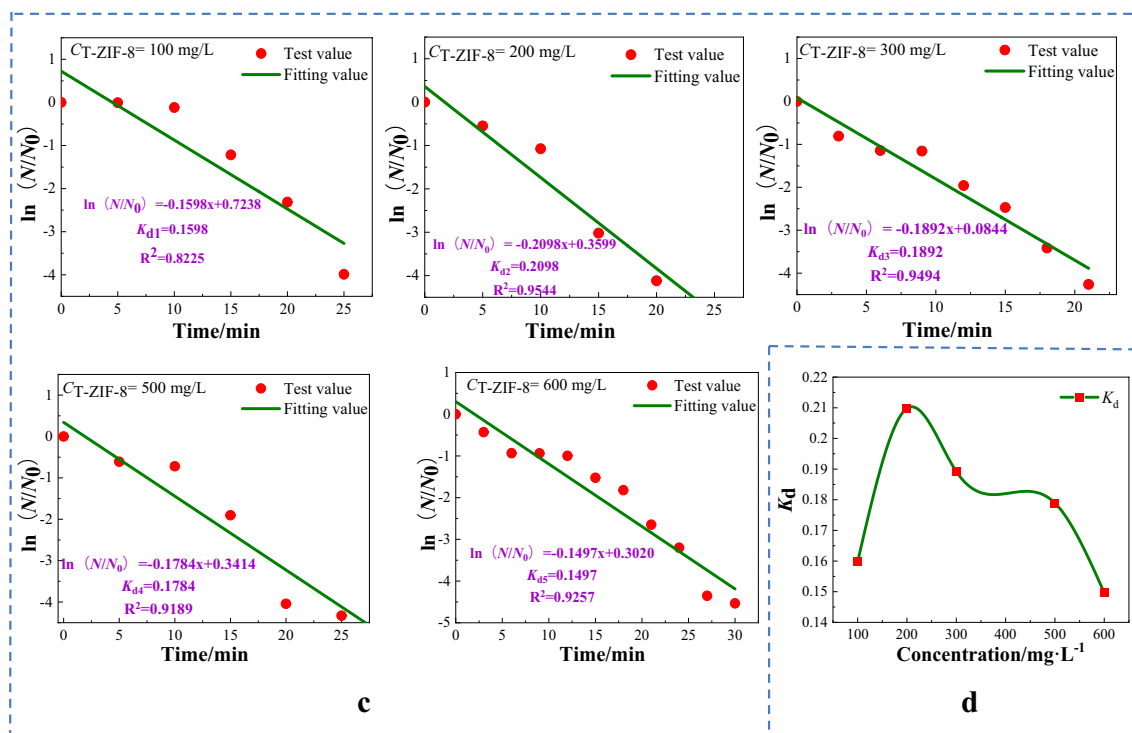
Fig. 8 (continued)

T-ZIF-8 is in Beta distribution with K_d, that is, the antibacterial behavior of T-ZIF-8-GP against *Escherichia coli* conforms to second-order kinetics.

According to the antibacterial results of T-ZIF-8-GP against *Staphylococcus aureus* and *Escherichia coli*, it is found that when the loading of T-ZIF-8 antibacterial agent on PP and melt-blown materials is 2%, the antibacterial rate of T-ZIF-8-GP against *Staphylococcus aureus* and *Escherichia coli* reaches the peak. *Staphylococcus aureus* and *Escherichia coli* are completely killed when the simulated sunlight is irradiated for 30 min, which is higher than the reported literature about ZIF-8 antibacterial agent [36]. When the loading of T-ZIF-8 is more than 2%, the antibacterial rate of T-ZIF-8-GP against both of bacteria decreases. It is due to the fact that the $\cdot O_2^-$ produced by T-ZIF-8-GP under the photocatalysis interacts with the proteins on the outer surface of bacteria, and the proteins gradually deform and solidify to form a protective shell on the outer surface of bacteria with the increase of the concentration of antibacterial agent [37]. Thus, the penetration rate of $\cdot O_2^-$ into the interior of microorganisms is reduced, leading to the decrease of the antibacterial rate ultimately.

In addition, the antibacterial rate of T-ZIF-8-GP against *Staphylococcus aureus* is significantly higher than that of *Escherichia coli*, because *Staphylococcus aureus* is belonged to Gram-positive bacteria and *Escherichia coli* is belonged to Gram-negative bacteria, and they have differences in cell structure and composition. The activity $\cdot O_2^-$ of T-ZIF-8-GP produced under photocatalytic conditions kills the bacteria by penetrating the bacterial cell wall and reacting with internal cellular components. The cell wall of Gram-negative bacteria is composed of thin peptidoglycan and outer membrane, and the outer membrane is mainly composed of lipopolysaccharide, lipoprotein and phospholipids. $\cdot O_2^-$ needs to penetrate the cell membrane by oxidating C=C in the outer membrane phospholipids to induce DNA oxidation, which makes $\cdot O_2^-$ transmission speed of bacterial cell wall drop. However, the cell wall of Gram-positive bacteria is mainly wrapped by porous peptidoglycan layer, $\cdot O_2^-$ can directly act on the inside of bacteria through the pore, thus accelerating the inactivation of superoxide free radical on bacteria.

3.8 Antibacterial Mechanism of Photocatalysis

Under the excitation of simulated sunlight, the electrons in the valence band are excited to the conduction band to generate photogenerated electron e^-, and the conduction band generates positively charged hole h^+, and a large number of photogenerated electron–hole pairs are finally formed in T-ZIF-8-GP. Under the action of electric field in the system, e^- and h^+ are separated and migrated to different positions on the surface of T-ZIF-8-GP. The photogenerated electron e^- is transferred from the ligand
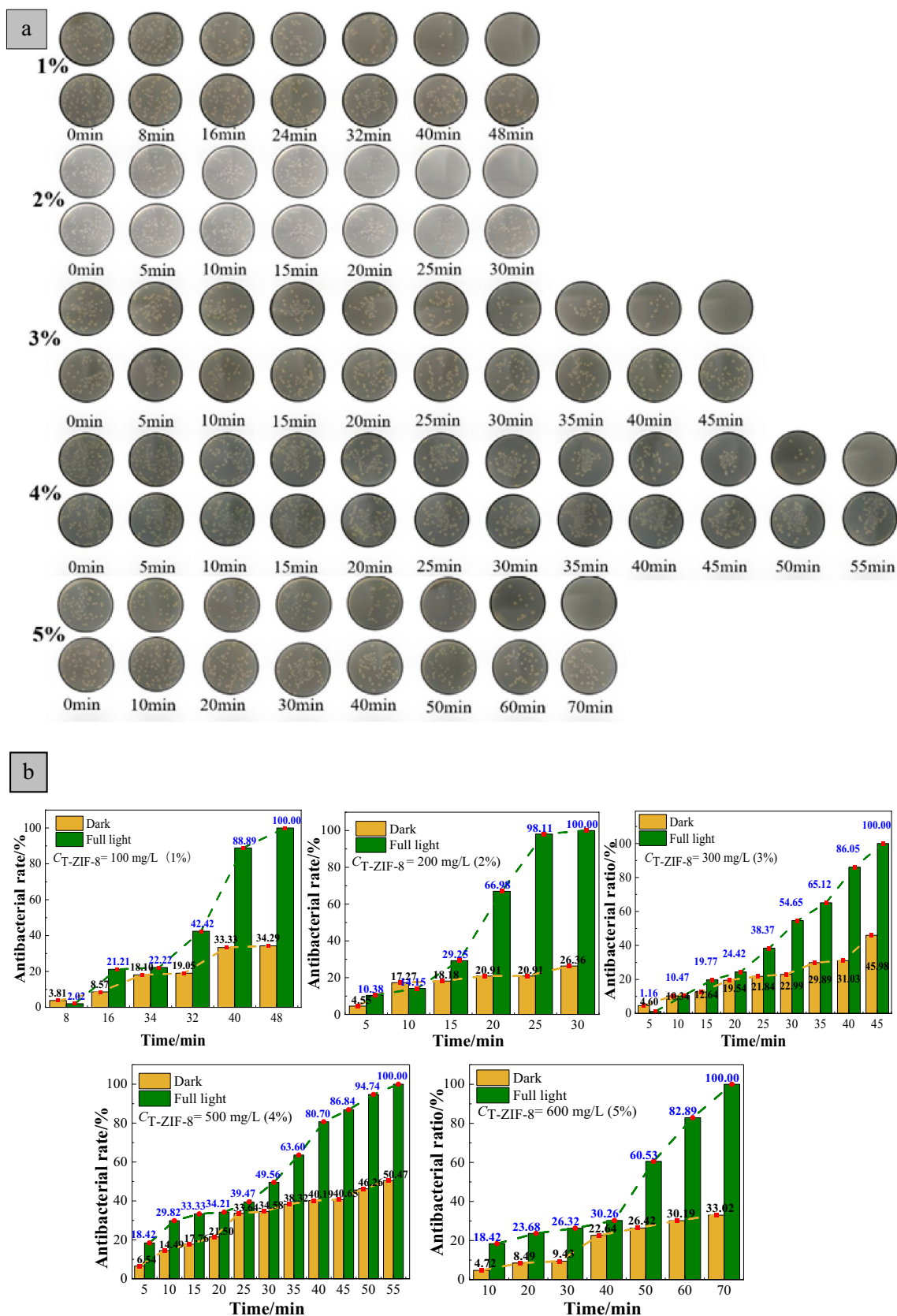
Fig. 9 Colony growth of *Escherichia coli* (**a**), the antibacterial ratio against *Escherichia coli* (**b**), the antimicrobial rate fitting curves (**c**) at different concentration of T-ZIF-8; the antibacterial dynamics fitting curve of T-ZIF-8-GP against *Escherichia coli* (**d**)
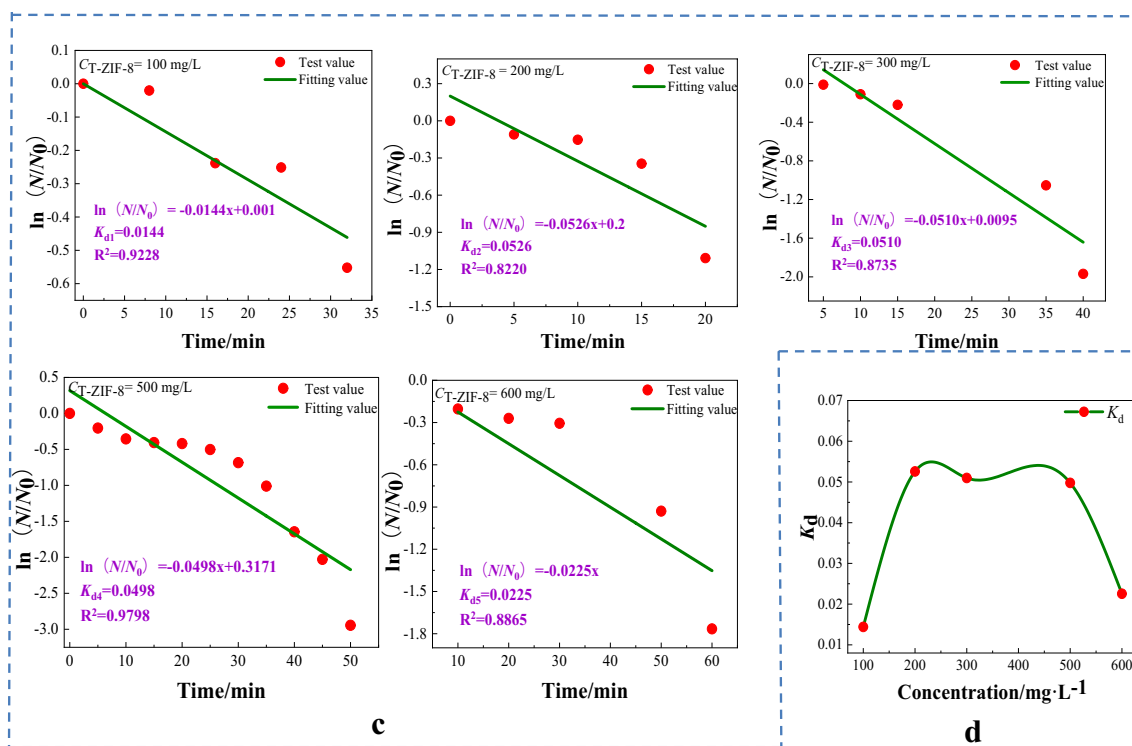
Fig. 9 (continued)

to the metal center Zn^{2+} by LMCT, and Zn^{2+} obtained the electrons are activated into Zn^+ with strong reducing property. Zn^+ reacts with O_2 in air or water, and Zn^+ is oxidized to Zn^{2+} and O_2 is reduced to $\cdot O_2^-$. $\cdot O_2^-$ with strong redox properties interacts with the hole (h^+) with strong oxidation to destroy the cell membrane, protein and genetic materials of bacteria, which makes it directly contact with the lipid of the bacterial membrane to induce the formation of pores on the outer membrane, resulting in the leakage of cytoplasmic contents. Finally, bacterial cells lysed and die [38, 39], and the bacterial remains and secretions are decomposed into non-toxic small molecules of CO_2 and H_2O [40], thus achieving self-cleaning bactericidal effects. The antibacterial mechanism diagram is depicted in Fig. 10.
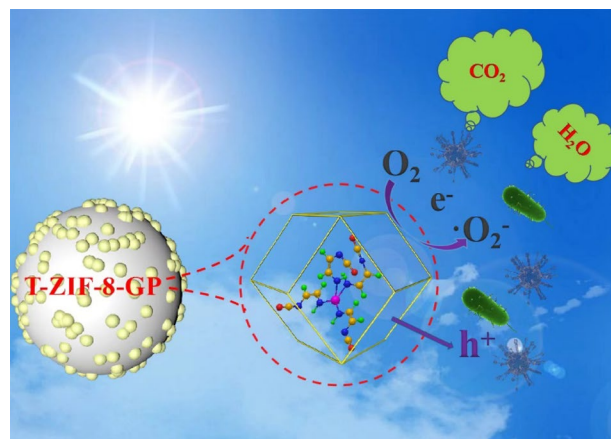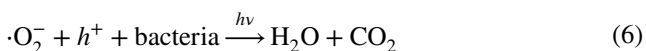
$$\text{T-ZIF-8-GP} \xrightarrow{h\nu} e^- + h^+ \tag{3}$$

$$e^- + Zn^{2+} \xrightarrow{\text{LMCT}} Zn^+ \tag{4}$$

$$Zn^+ + O_2 \rightarrow Zn^{2+} + \cdot O_2^- \tag{5}$$

$$\cdot O_2^- + h^+ + \text{bacteria} \xrightarrow{h\nu} H_2O + CO_2 \tag{6}$$

Fig. 10 Photocatalytic antimicrobial mechanism diagram of T-ZIF-8-GP

4 Conclusion

In this work, OL-AT1618 coupling agent was used to modify T-ZIF-8 antibacterial agent, which solved the agglomeration problem of T-ZIF-8 nanoparticles. Then, the modified T-ZIF-8-G was blended with PP and its melt-blown materials by the torque blending method to prepare the PP based antibacterial masterbatch, which maintained

the chemical structure of T-ZIF-8 and the thermal stability of PP. T-ZIF-8-GP basically maintains the photoresponse range of T-ZIF-8. Surprisingly, the band gap of T-ZIF-8-GP is significantly reduced, which promotes the generation rate of photogenerated electron–hole pairs and reduces the recombination rate under simulated sunlight irradiation, resulting in clearly improve photocatalytic performance. Photocatalytic antibacterial results against *Escherichia coli* and *Staphylococcus aureus* at different concentration of antibacterial agent suggest that the relationship between antibacterial rate and antibacterial agent concentration conform to the Beta distribution, displaying second-order kinetic behavior. The antibacterial activity reaches the peak when the loading of antibacterial agent T-ZIF-8 is 2% of the total mass of PP and melt-blown materials. The antibacterial rate of *Staphylococcus aureus* and *Escherichia coli* are completely killed when the sunlight irradiation for 30 min. The photocatalytic antibacterial mechanism of T-ZIF-8-GP is determined by energy level structure and free radical capture experiment. The photocatalytic antibacterial mechanism is revealed in which $\cdot O_2^-$ and h^+ as antibacterial active species.

Author Contributions QZ: Investigation, Data curation, Writing-original draft. QQ: Investigation, Data curation, Writing-original draft. ZW: Investigation, Formal analysis. YL: Investigation, Formal analysis. ZP: Investigation, Formal analysis. JG: Investigation, Formal analysis. PF: Conceptualization, Investigation. AZ: Supervision, Funding acquisition, Writing-review & editing. HJ: Conceptualization, Supervision, Writing—review & editing. BX: Supervision, Writing—review & editing.

Declarations

Conflict of interest The authors declare that they have no known competing financial interests or personal relationships that could have appeared to influence the work reported in this paper.

Research Involving Human and Animal Rights The research does not involve human participants and in vivo animals tests.

References

1. M. Reinhart, D. Metze, S.A. Braun, Skin manifestations of COVID-19 and after COVID-19 vaccination. Hautarzt **73**, 434–441 (2022)
2. J.W. Cao, F. Liu, M. Shang, X.T. Zhou, Toward street vending in post COVID-19 China: social networking services information overload and switching intention. Technol. Soc. **66**, 101669 (2021)
3. W.L. Oliani, F.H. Pusceddu, D.F. Parra, Silver-titanium polymeric nanocomposite non ecotoxic with bactericide activity. Polym. Bull. **79**, 10949–10968 (2022)
4. M. Naeem, M.B.M.C. Felipe, S.R.B. de Medeiros, T.H.C. Costa, M.S. Libório, C. Alves Jr. et al., Novel antibacterial silver coating on PET fabric assisted with hollow-cathodeglow discharge. Polym. Adv. Technol. **31**, 2896–2905 (2020)
5. I. Corsi, A. Bellingeri, M.C. Eliso, G. Grassi, G. Liberatori, C. Murano et al., Eco-interactions of engineered nanomaterials in the marine environment: towards an eco-design framework. Nanomaterials **11**, 1903 (2021)
6. H.T. Feng, X.J. Liu, Y. Li, X.Y. Ma, Q.L. Yan, F.Q. Zhao, Novel powder catalysts of ferrocene-based metal-organic framework and their catalytic performance for thermal decomposition of ammonium perchlorate. Powder. Technol. **397**, 117035 (2022)
7. T. Rasheed, K. Rizwan, M. Bilal, H.M.N. Iqbal, Metal-organic framework-based engineered materials-fundamentals and applications. Molecules **25**, 1598–1623 (2020)
8. J.D. Guo, H.S. Jia, A.Q. Zhang, Z. Pei, M. Luo, J.B. Xue et al., MIL-100 (Fe) with mix-valence coordinatively unsaturated metal site as Fenton-like catalyst for efficiently removing tetracycline hydrochloride: boosting Fe(III)/Fe(II) cycle by photoreduction. Sep. Purif. Technol. **262**, 18334 (2021)
9. J.D. Guo, A.Q. Zhang, Z. Pei, X.G. Liu, B.S. Xu, H.S. Jia, Efficient photo-Fenton degradation performance, mechanism, and pathways of tetracyc et line hydrochloride over missing-linker metal-organic framework with mix-valence coordinatively unsaturated metal sites. Sep. Purif. Technol. **287**, 120568 (2022)
10. S.A. Salim, A.A. Taha, E.E. Khozemy, S.H. EL-Moslamy, E.A. Kamoun, Electrospun zinc-based metal organic framework loaded-PVA/chitosan/hyaluronic acid interfaces in antimicrobial composite nanofibers scaffold for bone regeneration applications. J. Drug Deliv. Sci. Technol. **76**, 103823 (2022)
11. C.L. Yang, J. Wen, Z.Z. Xue, X.Y. Yin, Y.F. Li, L. Yuan, The accumulation and toxicity of ZIF-8 nanoparticles in *Corbicula fluminea*. J. Environ. Sci. **127**, 91–101 (2022)
12. L.C. Tan, G.S. Yuan, P. Wang, S.W. Feng, Y. Tong, C.J. Wang, pH-responsive Ag-Phy@ZIF-8 nanoparticles modified by hyaluronate for efficient synergistic bacteria disinfection. Int. J. Biol. Macromol. **206**, 605–613 (2022)
13. Z. Pei, P.F. Fei, A.Q. Zhang, J.D. Guo, J.C. Hao, J. Jia et al., Thermal oxygen sensitization modification and its visible light catalytic antibacterial performance for ZIF-8. J. Alloys Compd. **904**, 164055 (2022)
14. J.H. Ran, H.B. Chen, S.G. Bi, Q.F. Guo, Z.M. Deng, G.M. Cai et al., One-step in-situ growth of zeolitic imidazole frameworks-8 on cotton fabrics for photocatalysis and antimicrobial activity. Cellulose **27**, 10447–10459 (2020)
15. A. Kumar, A. Sharma, Y. Chen, M. Jones, S.T. Vanyo, C.N. Li et al., Copper@ZIF-8 core-shell nanowires for reusable antimicrobial face masks. Adv. Funct. Mater. **31**, 2008054 (2020)
16. Y.Y. Yang, Z.P. Guo, W. Huang, S.Y. Zhang, J.J. Hang, H.J. Yang et al., Fabrication of multifunctional textiles with durable antibacterial property and efficient oil-water separation via in situ growth of zeolitic imidazolate framework-8 (ZIF-8) on cotton fabric. Appl. Surf. Sci. **503**, 144079 (2020)
17. T. Lu, H.B. Liang, W.X. Cao, Y.K. Deng, Q.L. Qu, W.J. Ma et al., Blow-spun nanofibrous composite self-cleaning membrane for enhanced purification of oily wastewater. J. Colloid Interface Sci. **608**, 2860–2869 (2022)
18. T.T. Li, Y.J. Fan, X.X. Cen, Y. Wang, B.C. Shiu, H.T. Ren et al., Polypropylene/polyvinyl alcohol/metal-organic framework-based melt-blown electrospun composite membranes for highly efficient filtration of PM2.5. Nanomaterials **10**, 2025 (2020)

19. J.X. Guo, A. Hanif, J. Shang, B.J. Deka, N. Zhi, A.K. An, PAA@ ZIF-8 incorporated nanofibrous membrane for high-efficiency PM 2.5 capture. Chem. Eng. J. **405**, 126584 (2021)

20. J. Fonseca, T.H. Gong, L. Jiao, H.L. Jiang, Metal-organic frameworks (MOFs) beyond crystallinity: amorphous MOFs, MOF liquids and MOF glasses. Mater. Chem. A **9**, 10562–10611 (2021)

21. N. Gowriboy, R. Kalaivizhi, M.R. Ganesh, K.A. Aswathy, Development of thin film polymer nanocomposite membrane (ZIF-8@ PSf/CS) for removal of textile pollutant and evaluating the effect of water samples on human monocytic cell lines (THP-1) using flow cytometer. J. Clean. Prod. **377**, 134399 (2022)

22. L.L. Wang, *Synthesis and Application of Al–Ti Coupling Agent* (Shanxi University of Science and Technology, Xi'an, 2012)

23. H. Zhou, J. Xiang, Y. Li, J.R. Zhong, Y.F. Zhang, The nucleation mechanism of 1-N′,3-N′-dibenzoylbenzene-1,4-dicarbohydrazide as a nucleating agent for isotactic polypropylene. J. Polym. Res. **29**, 283 (2022)

24. O. Yagci, G.B. Eker, M. Tasdemir, Thermal, structural and dynamical mechanical properties of hollow glass sphere-reinforced polypropylene composites. Polym. Bull. **78**, 3089–3101 (2020)

25. B. Wang, R. Utzeri, M. Castellano, P. Stagnaro, A.J. Muller, D. Cavallo, Heterogeneous nucleation and self-nucleation of isotactic polypropylene microdroplets in immiscible blends: from nucleation to growth-dominated crystallization. Macromolecules **53**, 5980–5991 (2020)

26. X.W. Wang, Z.Q. Cao, B. Du, Y. Zhang, R.B. Zhang, Visible-light-driven zeolite imidazolate frameworks-8@ZnO composite for heavy metal treatment. Composites B **183**, 107685 (2020)

27. H. Chen, Y.Q. Wang, F. Huang, C. Tu, L. Cui, Layer by layer self-assembly MoS$_2$/ZIF-8 composites on carboxyl cotton fabric for enhanced visible light photocatalysis and recyclability. Appl. Surf. Sci. **565**, 150458 (2021)

28. T. Li, X. Guo, L.J. Zhang, T. Yan, Z.L. Jin, 2D CoP supported 0D WO$_3$ constructed S-scheme for efficient photocatalytic hydrogen evolution. Int. J. Hydrogen Energy **46**, 20560–20572 (2021)

29. S.N.S. Nasir, N.A. Mohamed, M.A. Tukimon, M.F.M. Noh, N.A. Arzaee, M.A.M. Teridi, Direct extrapolation techniques on the energy band diagram of BiVO$_4$ thin films. Phys. B: Condens. Matter **604**, 412719 (2021)

30. G.H. Zuo, A.Q. Wang, Y. Yang, H.L. Huang, F.B. Wang, H.W. Jiang et al., Fabrication and characterization of Ag/AgCl@ZIF-8 hybrid nanostructure and used its as photocatalyst for degradation of rhodamine B under visible light. J. Porous Mater. **27**, 339–345 (2020)

31. R.G. Yang, Y.M. Fu, H.N. Wang, D.P. Zhang, Z. Zhou, Y.Z. Cheng et al., ZIF-8/covalent organic framework for enhanced CO$_2$ photocatalytic reduction in gas-solid system. Chem. Eng. J. **450**, 138040 (2022)

32. A. Al Mayyahi, B.M. Everhart, T.B. Shrestha, T.C. Back, P.B. Amama, Enhanced charge separation in TiO$_2$/nanocarbon hybrid photocatalysts through coupling with short carbon nanotubes. Rsc. Adv. **11**, 11702–11713 (2021)

33. Y. Zhou, S. Feng, X. Duan, W. Wu, Z.W. Ye, X.G. Dai et al., Stable self-assembly Cu$_2$O/ZIF-8 heterojunction as efficient visible light responsive photocatalyst for tetracycline degradation and mechanism insight. J. Solid State Chem. **305**, 122628 (2021)

34. T.Y. Fan, Y. Ren, Z.Y. Zhao, Preparation and antibacterial properties of Ag$_6$Si$_2$O$_7$–TiO$_2$/PP composite photocatalytic materials. Chin. J. Compos. Mater. **39**, 3915–3921 (2022)

35. L. Jasinska-Walc, M. Bouyahyi, P. Lorenc, A.L. Heeneman, R. Duchateau, A. Rozanski et al., Synthesis of isotactic polypropylene-block-polystyrene block copolymers as compatibilizers for isotactic polypropylene/polyphenylene oxide blends. Polymer **147**, 121–132 (2018)

36. P. Li, J.Z. Li, X. Feng, J. Li, Y.C. Hao, J.W. Zhang, H. Wang, A.X. Yin, J.W. Zhou, X.J. Ma, B. Wang, Metal-organic frameworks with photocatalytic bactericidal activity for integrated air cleaning. Nat. Commun. **10**, 2177 (2019)

37. J.M. Boyce, Alcohols as surface disinfectants in healthcare settings. Infect. Control Hosp. Epidemiol. **39**, 323–328 (2018)

38. Y.P. Li, Q. Wang, L.Y. Huang, X.Q. Xu, M. Xie, H. Wang et al., Enhanced LED-light-driven photocatalytic antibacterial by g-C$_3$N$_4$/BiOI composites. J. Mater. Sci.: Mater. Electron. **30**, 2783–2794 (2019)

39. J.X. Ruan, H.M. Pei, T. Li, H.Y. Wang, S.F. Li, X.R. Zhang, Preparation and antioxidant activity evaluation of tea polyphenol-collagen-alginate microspheres. J. Food Process. Preserv. **45**, e15187 (2021)

40. Y.F. Chen, X.N. Tang, X. Gao, B. Zhang, Y. Luo, X.Y. Yao, Antimicrobial property and photocatalytic antibacterial mechanism of the TiO$_2$-doped SiO$_2$ hybrid materials under ultraviolet-light irradiation and visible-light irradiation. Ceram. Int. **45**, 15505–15513 (2019)

Publisher's Note Springer Nature remains neutral with regard to jurisdictional claims in published maps and institutional affiliations.